Monthly Notices
of the
ROYAL ASTRONOMICAL SOCIETY

Mon. Not. R. Astron. Soc. **402,** 259–270 (2010) doi:10.1111/j.1365-2966.2009.15923.x

The parsec-scale distributions of intensity, linear polarization and Faraday rotation in the core and jet of Mrk 501 at 8.4–1.6 GHz

S. M. Croke,[1] S. P. O'Sullivan[2⋆] and D. C. Gabuzda[2]

[1]*Perimeter Institute for Theoretical Physics, 31 Caroline St. N, Waterloo, Ontario N2L 2Y5, Canada*
[2]*Physics Department, University College Cork, Cork, Ireland*

Accepted 2009 October 22. Received 2009 October 17; in original form 2009 July 16

ABSTRACT

Previous very long baseline interferometry (VLBI) observations of the nearby ($z = 0.0337$) active galactic nucleus (AGN) Mrk 501 have revealed a complex total-intensity structure with an approximately 90° misalignment between the jet orientations on parsec and kiloparsec scales. The jet displays a 'spine' of magnetic field orthogonal to the jet surrounded by a 'sheath' of magnetic field aligned with the jet. Mrk 501 is also one of a handful of AGN that are regularly detected at TeV energies, indicating the presence of high-energy phenomena in the core. However, multi-epoch analyses of the VLBI total-intensity structure have yielded only very modest apparent speeds for features in the VLBI jet. We investigate the total-intensity and linear-polarization structures of the parsec- to decaparsec-scale jet of Mrk 501 using VLBA observations at 8.4, 5, 2.2 and 1.6 GHz. The rotation-measure distribution displays the presence of a Faraday rotation gradient across an extended stretch of the jet, providing new evidence for a helical magnetic field associated with the jet of this AGN. The position of the radio core from the base of the jet follows the law $r_{\rm core}(\nu) \propto \nu^{-1.1\pm0.2}$, consistent with the compact inner jet region being in equipartition. Hence, we estimate a magnetic field strength of ∼40 mG at a distance of 1 pc.

Key words: galaxies: active – galaxies: jets – galaxies: magnetic fields.

1 INTRODUCTION

The radio emission of core-dominated, radio-loud active galactic nuclei (AGN) is synchrotron radiation generated in the relativistic jets that emerge from the nucleus of the galaxy, presumably along the rotational axis of a central supermassive black hole.

Mrk 501 is an object from the catalogue of E.B. Markarian and colleagues at the Byurakan Observatory in Armenia, which selects sources with unusually strong ultraviolet continua. Details of the survey undertaken in order to compile this catalogue, together with the selection criteria, are given by Lipovetsky, Makarian & Stepanian (1987). The host galaxy of the AGN is an elliptical galaxy, whose redshift is modest, $z_{\rm gal} = 0.0337$ (Ulrich et al. 1975). It has been classified as a high-energy-peaked BL Lac object, with its synchrotron emission peak in the ultraviolet/soft X-ray (Giommi & Padovani 1994; Padovani & Giommi 1995). The relative proximity of Mrk 501 means that more structural detail can be resolved with the angular resolution available from current observational techniques than is the case for more distant AGN.

The parsec-scale total-intensity structure of Mrk 501 is well studied at radio wavelengths. On arcsec scales, Very Large Array (VLA) images show a two-sided structure oriented in position angle (measured from north through east) PA∼45° (e.g. Kollgaard et al. 1992; Cassaro et al. 1999). Arcsec angular scales in Mrk 501 correspond to kpc linear scales in the plane of the sky. The higher angular resolutions provided by very long baseline interferometry (VLBI) enable studies of the source structure on parsec (milliarcsecond) scales (Aaron 1999; Giovannini et al. 1999; Giroletti et al. 2004, 2008). At this resolution, a one-sided, core-jet structure is revealed, with a complex jet morphology. The inner jet emerges at a PA of ∼145°–155°, but bends several times before a final change in direction to a PA of ∼45°, in agreement with the lower resolution VLA images. The jet also opens out considerably at this point to form a cone of diffuse emission. This complex behaviour may be due to interaction with the surrounding medium, forcing the jet to bend. A helical jet, such as that invoked by Conway & Wrobel (1995) to explain the roughly orthogonal misalignment between the parsec and kpc scale structure, could also explain the complex jet morphology, but evidence in support of this hypothesis is not conclusive.

Despite being one of the few AGN that are regularly detected at TeV energies (e.g. Djannati-Ataı et al. 1999; Yamamoto et al. 1999), clearly indicating the presence of very high energy phenomena occurring in its core, the jet morphology shows little variation with time. Multi-epoch analyses of the VLBI total-intensity structure have yielded only subluminal speeds for features in the VLBI

⋆E-mail: shaneosullivan@phys.ucc.ie

jet (Edwards & Piner 2002; Giroletti et al. 2004). One possibility is that the low component speeds are an artefact due to the fact that the time intervals between observing epochs have been too large to reliably track very rapid evolution of individual features. However, there is some evidence that high-energy-peaked BL Lac objects display typical superluminal speeds lower than those of low-energy-peaked (roughly speaking, radio-selected) BL Lac objects and quasars (Kharb, Gabuzda & Shastri 2008), suggesting that the low component speeds most likely reflect a comparatively low intrinsic outflow speed for the jet.

The polarization properties of this source are less well studied, but have been considered by various authors (Aaron 1999; Pushkarev et al. 2005; Giroletti et al. 2008). The polarization structure is complex and shows a 'spine+sheath' structure, i.e. a spine of polarization electric (***E***) vectors *aligned* with the VLBI jet in the central part of the jet, surrounded by a sheath of *orthogonal* ***E*** vectors at the edges of the jet. In optically thin regions, the magnetic (***B***) field is generally close to perpendicular to the observed ***E*** vectors.[1] The spine and sheath configuration therefore implies a ***B*** field that is transverse to the jet near the ridge line and aligned with the jet at its edges. This has previously been interpreted to be due to the presence of a spine of fast moving plasma and a slower shear layer that forms due to interaction with the surrounding environment (Aaron 1999). In this picture, shocks propagating through the fast moving plasma would compress material in the jet spine, enhancing the transverse ***B***-field component (e.g. Laing 1980; Hughes, Aller & Aller 1989). In the slower shear layer, the longitudinal component of the ***B*** field is stretched due to interaction of the fast material near the central part of the jet and the surrounding medium. Alternatively, the observed polarization could be due to a helical ***B*** field, without any need to invoke a shear layer (Gabuzda, Pushkarev & Cawthorne 2000; Lyutikov et al. 2005; Pushkarev et al. 2005). In this picture, the transverse and aligned ***B*** fields are attributed to toroidal and poloidal components of the projection of a helical field on to the sky, which predominate near the central axis and near the edges of the jet, respectively.

We assume throughout a cosmology with $H_0 = 71\,\mathrm{km\,s^{-1}\,Mpc^{-1}}$, $\Omega_\mathrm{M} = 0.27$ and $\Omega_\Lambda = 0.73$ (Wright 2006).

2 ANALYSIS TECHNIQUES USED

2.1 Spectral index mapping

Spectral index maps can be constructed by comparing the emission from a source at two frequencies ν_1 and ν_2. The spectral index is then simply a measure of the relative flux at the two frequencies at any given point:

$$\alpha = \frac{\ln(I_{\nu_1}/I_{\nu_2})}{\ln(\nu_1/\nu_2)}, \tag{1}$$

where I_ν is the intensity measured at that point at frequency ν and $I(\nu) \propto \alpha$. The spectral index varies spatially throughout the source. The radio core is expected to be at least partially optically thick at most frequencies, since absorption is especially efficient in the dense regions near the base of the jet. The less dense extended emission usually has a relatively steep spectrum ($\alpha \simeq -0.5$ to -1.0) at higher radio frequencies (8–22 GHz), turning over to yield flat or positive spectra at low frequencies (at or below 5 GHz), where absorption is more efficient.

[1] While the analysis of Lyutikov, Pariev & Gabuzda (2005) shows that this is not, in general, strictly true, it will be the case for observations with modest resolution (effectively averaging over the cross-section of the jet) for jets with roughly cylindrical symmetry. Therefore, while bearing in mind the caution that must be applied to detailed analyses, we will assume that the observed ***E*** vectors in our images are orthogonal to the associated ***B*** field.

2.2 Faraday rotation mapping

When plane polarized light travels through a magnetic field, the plane of polarization is rotated as a result of its interaction with the external ***B*** field. This effect is known as Faraday rotation. Faraday rotation occurring in our own Galaxy is expected to be uniform over scales of several tens of mas (or more) on the sky, while Faraday rotation in the immediate vicinity of the source could vary spatially throughout the source.

For radiation at wavelength λ, the angle through which the plane of polarization is rotated is proportional to λ^2. The constant of proportionality rotation measure (RM) depends on the component of the magnetic field along the line of sight $\boldsymbol{B} \cdot \mathrm{d}\boldsymbol{s}$ and the plasma density along the line of sight $N(s)$. This relationship is given by (e.g. Spitzer 1978; Sturrock 1994):

$$\Delta\chi = \mathrm{RM}\lambda^2 = \frac{e^3\lambda^2}{8\pi^2 m_\mathrm{e}^2 \epsilon_0 c^3} \int N(s)\boldsymbol{B}(\boldsymbol{s}) \cdot \mathrm{d}\boldsymbol{s},$$

where e is the electron charge, m_e the electron mass, ϵ_0 the electrical permittivity in free space and c the speed of light in vacuum, and the integral is taken along the line of sight from the source to the observer (i.e. along the path travelled by the observed radiation). Note that we specify the electron as the relevant charge, since the inverse dependence on the particle mass squared implies that Faraday rotation by thermal electrons will be much stronger than Faraday rotation by either protons or relativistic electrons (whose effective mass is γm_e^2, where γ is the Lorentz factor for their motion).

Thus, Faraday rotation will be detected anywhere the ***B*** field has a non-zero component along the line of sight, and variations in the RM throughout the source can be taken to indicate differences in the magnetic field and/or electron density along the various lines of sight. For example, the line-of-sight component of a helical jet magnetic field varies across the jet, giving rise to a characteristic gradient in the RM across the jet. Note that while variations in electron density could also produce RM gradients, it is difficult to explain changes in the sign of the RM across the jet, such as have been observed for several AGN, including Mrk 501 (Gabuzda, Murray & Cronin 2004), in this way. Thus, a systematic RM gradient across the jet provides compelling evidence for a helical magnetic field, particularly if the gradient encompasses both positive and negative RM values.

3 THE CURRENT STUDY

We investigate here the total-intensity and linear-polarization structures of the parsec- to decaparsec-scale jet of Mrk 501 using VLBA observations obtained in 1998 May at 8.4, 5, 2.2 and 1.6 GHz. We consider both the spectral index and Faraday RM distributions, as well as an analysis of the frequency-dependent VLBI core shift. The spectral index distributions are complex and display appreciable variations both across and along the jet. The RM distribution displays a transverse RM gradient along an extended stretch of the jet, providing clear evidence for a helical ***B*** field associated with the Mrk 501 jet. The position of the radio core from the base of the jet follows the law $r_\mathrm{core}(\nu) \propto \nu^{-1.1\pm0.2}$, consistent with the compact inner jet of Mrk 501 being in equipartition.

4 OBSERVATIONS AND CALIBRATION

The VLBA polarization observations considered here, which we acquired from the VLBA archive, were obtained at 5, 8.4, 2.2 and 1.6 GHz on 1998 May 15 and 20 (see Table 1). Observations were also made for the same project at 15.4 and 22.2 GHz, but our results at these frequencies will be presented in a separate paper. Thus, the data for 5 and 8.4 GHz (May 15) and for 1.6 and 2.2 GHz (May 20) were obtained virtually, but not strictly, simultaneously. The *uv*-planes at each frequency are plotted in Fig. 1. We found no evidence that the source had varied in the five days between the observations for the two highest and two lowest frequencies. This is among the first VLBI polarization studies of AGN at frequencies as low as 1.6 and 2.2 GHz (e.g. Gabuzda & Chernetskii 2003; Pushkarev et al. 2005; Hallahan & Gabuzda 2008).

Table 1. Summary of observations.

Observation date	Frequencies (MHz)
1998 May 15	4987.490, 8421.490, 15 365.490*
1998 May 20	1659.459, 2271.459, 22 233.459*

*Results for these frequencies presented in a separate paper.

The preliminary calibration, polarization calibration and imaging of the data were done fully in the National Radio Astronomy Observatory (NRAO) AIPS package using standard techniques. The compact polarized source 1823+568 was observed as a polarization calibrator at all frequencies; a joint solution for the instrumental polarizations ('D-terms') and the source polarization was obtained using the AIPS task LPCAL. We obtained all total-intensity (I) images of Mrk 501 and the calibrator 1823+568 using the AIPS tasks CALIB and IMAGR in an interative fashion. Once the visibility data were fully self-calibrated, we also made maps of the distribution of the Stokes parameters Q and U, which were then input to the AIPS task COMB to produce the corresponding distributions of the polarized flux $p = mI$ (PPOL), where m is the degree of polarization and the

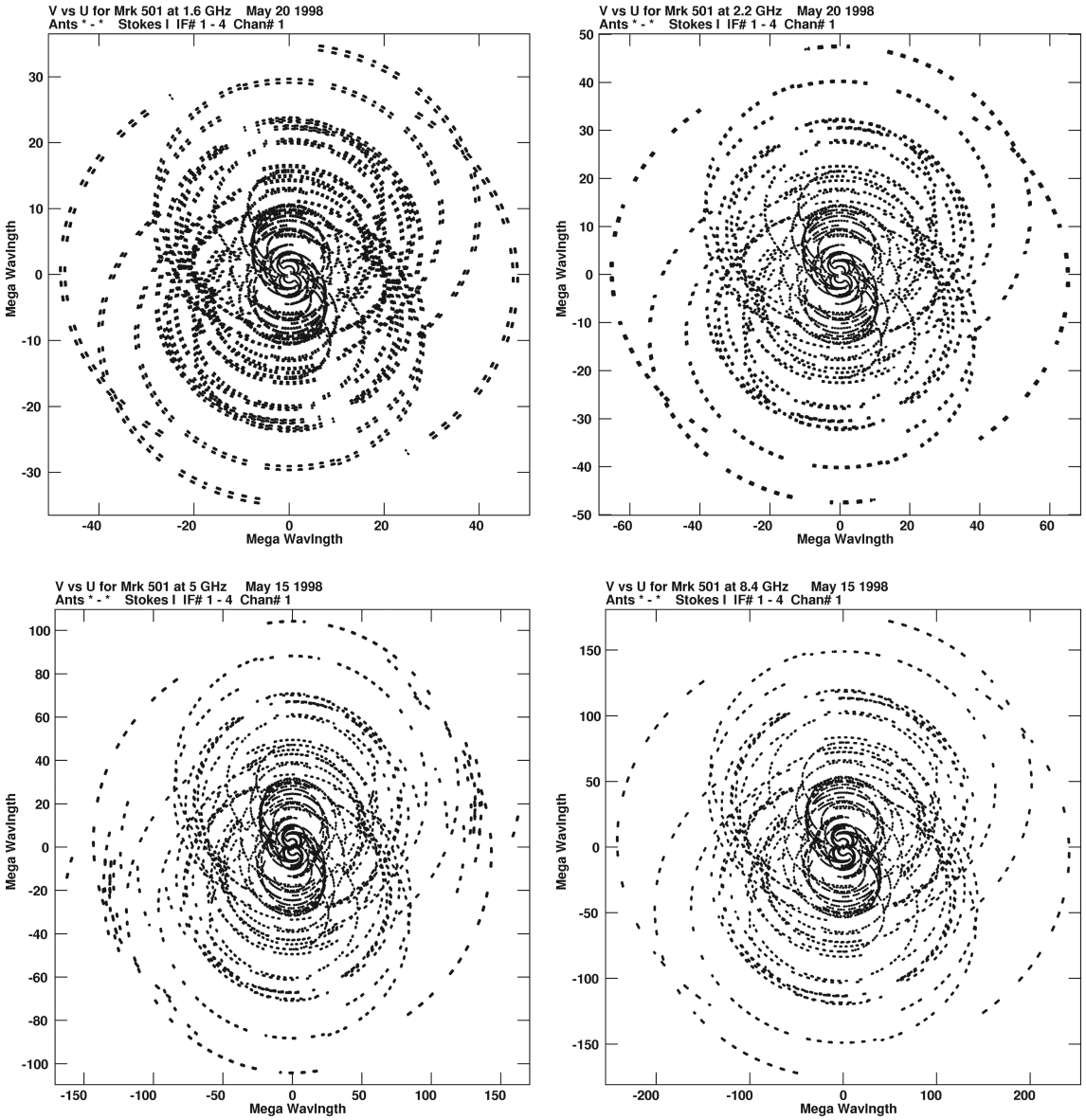

Figure 1. Plots of uv planes at each frequency. Top-left panel: 1.6 GHz (1998 May 20), top-right panel: 2.2 GHz (1998 May 20), bottom-left panel: 5 GHz (1998 May 15), bottom-right panel: 8.4 GHz (1998 May 15).

electric vector position angle (EVPA) $\chi = 0.5 \arctan(U/Q)$ [polarization angle (PANG)].

The standard procedure for calibrating the EVPAs is to compare the (quasi-)simultaneously measured integrated polarization of a compact source with the total polarization on VLBI scales, rotating the PANGs for the VLBI data so that the EVPAs for the integrated and total VLBI polarizations coincide. The NRAO maintains a data base of integrated polarization data that can be used for this purpose (http://www.vla.nrao.edu/astro/calib/polar/), but 1823+568 is not among the sources monitored in this program. We also had at our disposal single-dish polarization measurements obtained at the University of Michigan Radio Astronomy Observatory (UMRAO), kindly provided by M. Aller (UMRAO; http://www.astro.lsa.umich.edu/obs.radiotel/umrao.html). We used UMRAO measurements of 1823+568 at 5 GHz on 1998 May 11 (only 4 days before our data) to determine the EVPA calibration for our 5 GHz data, but the UMRAO data at 8.4 were more variable and not as close in time, leading to concerns about polarization variability between the UMRAO and VLBA epochs. Fortuitously, the VLBA observations occurred only about 3.5 weeks after the third epoch of VLBA polarization observations of Charlot et al. (2006) at 5, 8, 15 and 22 GHz. The rotation that must be applied to calibrate the VLBA EVPAs is equal to the right–left phase difference of the reference antenna used in the preliminary data reduction and is typically stable on timescales of months, or even years (e.g. Reynolds, Cawthorne & Gabuzda 2001, http://www.physics.purdue.edu/astro/MOJAVE/). Accordingly, since we used the same reference antenna as Charlot et al. (2006) (Los Alamos), and since the last epoch of that work and our own observations was separated by only a few weeks, we were able to apply the EVPA calibration of Charlot et al. (2006) directly. The 5-GHz EVPA calibration derived using the UMRAO data was in excellent agreement with the 5-GHz EVPA calibration of Charlot et al. (2006), and the EVPA correction of Charlot et al. (2006) for 8.4 GHz gave fully consistent results for our 1823+568 polarization image at that frequency.

This left us with the task of calibrating the absolute EVPAs for the 2.2- and 1.6-GHz data, for which no integrated measurements were available. To do this, we constructed linear-polarization maps of 1823+568 using the calibrated 5- and 8.4-GHz data, identified a region in the VLBI jet approximately 8 mas from the VLBI core where polarization was clearly detected at 5.0, 8.4, 2.2 and 1.6 GHz (see Fig. 2) and verified that the small offset between the calibrated 5- and 8-GHz EVPAs in this region was consistent with the expected offset due to the known integrated (presumed Galactic) Faraday rotation of this object ($+35$ rad m^{-2}, leading to a rotation of $+4\overset{\circ}{.}6$ between 5.0 and 8.4 GHz; Pushkarev 2001). We further derived the *intrinsic* EVPA for this region of the source by extrapolating to zero wavelength using the observed 5.0- and 8-GHz EVPAs χ and the corresponding Faraday RM: $\chi_0 = \chi - \mathrm{RM}\lambda^2$, as is shown in Table 2. We then calculated the Faraday rotations at 2.2 and 1.6 GHz and the expected observed EVPAs for this region in 1823+568 at 2.2 and 1.6 GHz, using these rotations and the derived intrinsic EVPA (Table 2). Finally, we were able to derive the EVPA rotations required to calibrate the EVPAs at 2.2 and 1.6 GHz by comparing the expected and actual observed EVPAs at these frequencies in this part of the VLBI jet. In all cases, the orientation of the EVPAs in the selected location in the 1823+568 jet was determined using the AIPS verb IMSTAT. The RM distributions for 1823+568 constructed from the resulting calibrated data were consistent with a negligible RM in regions of appreciable polarization in the VLBI jet, as expected (Zavala & Taylor 2003). A summary of the EVPA calibrations used for the four frequencies for which we present results here is given in Table 2.

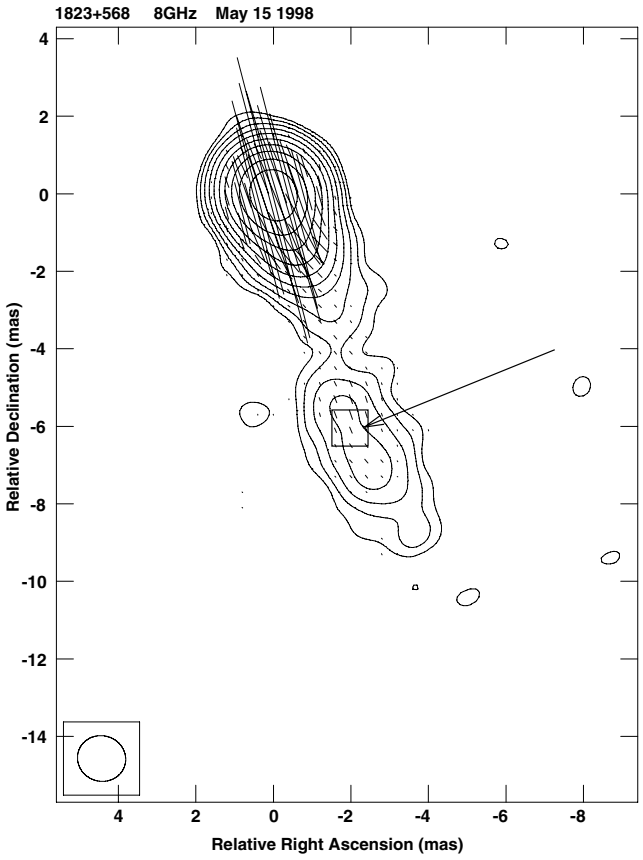

Figure 2. Contours of total intensity of 1823+568 at 8.4 GHz. The region used for the calibration of the EVPAs at 1.6 and 2.2 GHz is marked.

Table 2. Summary of information for EVPA calibration.

Determining χ_0 for the region in Fig. 2 at 5.0 and 8.4 GHz			
Frequency (GHz)	$\chi_{\mathrm{obs}}(^\circ)$	$-\mathrm{RM}_{\mathrm{int}}\,\lambda^2(^\circ)$	$\chi_0(^\circ)$
5.0	+26	−7	+19
8.4	+23	−3	+20
Determining the expected EVPAs at 1.6 and 2.2 GHz, χ_{exp}			
Frequency (GHz)	$\chi_0(^\circ)$	RM λ^2 $(^\circ)$	$\chi_{\mathrm{exp}}(^\circ)$
1.6	+19	+65	+84
2.2	+19	+34	+53

Derived EVPA corrections $\Delta\chi$	
Frequency (GHz)	$\Delta\chi$ $(^\circ)$
5.0	−62
8.4	−47
2.2	+110
1.6	+87

5 OBSERVATIONAL RESULTS

The images obtained are shown in Figs 3–4, which present *I* contour maps with superposed sticks representing the intensity and direction of the ***E*** vectors χ of the linearly polarized emission, and in Figs 5–6, which present *I* contour maps at 2.2 and 1.6 GHz for a larger region

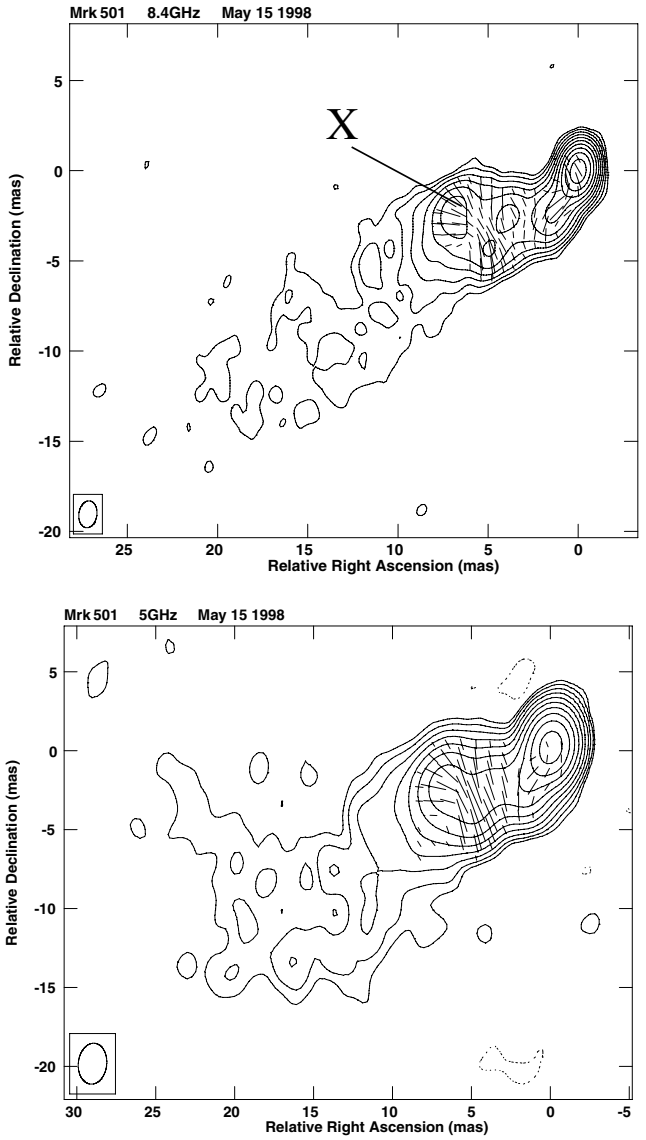

Figure 3. Contours of total intensity at 8.4 GHz (top panel) and 5 GHz (bottom panel) with superposed polarization $\boldsymbol{E}$ vectors. The convolving beams have FWHM 1.5×1.0 mas in PA $= -8^\circ$ (left) and 2.6×1.8 mas in PA $= -6^\circ$ (right). The contour levels are -0.7, 0.7, 1.4, 2.8, 5.6, 11.2, 22.4, 44.8, 89.6, 179.2 and 358.0 mJy beam^{-1}, and the peaks are 586.3 (left) and 532.3 mJy beam^{-1} (right). The $\boldsymbol{E}$ vectors have been rotated by $-\mathrm{RM}_{\mathrm{int}}\lambda^2 = -4^\circ$ (top panel) and -9° (bottom panel) to remove the integrated Faraday rotation.

displaying the extended jet structure detected at these frequencies. We also include a 2.2 GHz image tapered to match the 1.6 GHz resolution (Fig. 7). In all cases, the observed polarization vectors have been rotated by $-\mathrm{RM}_{\mathrm{int}}\lambda^2$ using the value of $\mathrm{RM}_{\mathrm{int}}$ derived by Rusk (1988), +42 rad m^{-2}, to remove the effect of the integrated (Galactic) RM. The full width at half-maximum (FWHM) of the restoring beams used is given in each caption and shown in the bottom-left corner of each image.

5.1 Total-intensity structure

Fig. 3 shows our maps of Mrk 501 at 8.4 and 5 GHz. The complex jet morphology is consistent with that observed in previous studies. The VLBI jet emerges at a PA of $\sim 150^\circ$, but by ~ 4 mas from the core has changed direction to a PA of $\sim 90^\circ$. From the images shown here, this part of the VLBI jet cannot be said to be limb brightened, as reported by Giroletti et al. (2004).

At ~ 8 mas from the core, the VLBI jet changes direction again, and this portion of the jet appears limb-brightened in the 8.4 GHz image. The jet also begins to lose collimation in this region, with the emission becoming increasingly diffuse. A region of enhanced emission can be seen just before this bend at 8.4 GHz (labelled X in Fig. 3). It is possible that interaction with the surrounding medium causes both the bending of the jet here and an enhancement of the density of relativistic electrons, causing the observed increase in the intensity of synchrotron radiation.

A hint of the final change in direction, at ~ 20–30 mas from the core, can be seen in the 5 GHz data; this dramatic, approximately right-angle bend can be seen clearly in the lower frequency images (Figs 4–6). The jet partially loses collimation here and opens to form a cone of emission aligned with that seen at lower angular resolution.

Interestingly, our 2.2- and 1.6-GHz images show further emission at a distance of 160–180 mas from the core, most clearly seen at 2.2 GHz (Figs 5 and 7). This may be why it has not been previously detected in other observations with comparable sensitivity and resolution, as the most comprehensive study of this source at radio frequencies to date, that of Giroletti et al. (2004), included data at 1.6, 5, 8.4, 15 and 22 GHz, but not 2.2 GHz. The emission at this distance from the core in the high-sensitivity image of Giroletti et al. (2008) is clearly stronger at the north-western edge of the jet, consistent with our 2.2- and 1.6-GHz images. This may be associated with further 'wiggling' of the jet, or possibly interaction between the jet and surrounding medium.

The VLBI total-intensity structure seen in the 8.4–1.6-GHz images can be explained by a helical jet model such as that proposed by Conway & Wrobel (1995), but the evidence for this is not convincing from the jet morphology alone.

5.2 Polarization structure

The jet polarization structure at our observing epoch is dominated by transverse polarization, although a central region of longitudinal (aligned) polarization vectors can be seen in the inner jet at 8.4 GHz. We have detected appreciable polarization in the extended emission at 2.2 and 1.6 GHz. Roughly transverse polarization can be seen at the southern edge of the jet as far as 30 mas from the core at both 1.6 and 2.2 GHz. The central spine of longitudinal polarization can also be seen at these frequencies, ~ 15–20 mas from the core. The sheath of perpendicular polarization remains orthogonal to the VLBI jet as the jet bends, even as it undergoes an almost right-angle bend $\simeq 20$–30 mas from the core. Note that the direction of the observed polarization at 1.6 and 2.2 GHz may be affected by residual Faraday rotation nearby the source, since the amount of rotation is proportional to λ^2. Thus, although the polarization vectors shown at the two higher frequencies are probably close to their intrinsic orientations, those at 1.6 and 2.2 GHz may remain rotated by a non-negligible amount. We present low-frequency polarization images corrected for this local Faraday rotation in Fig. 4.

5.3 Spectral index maps

We constructed spectral index maps for the three pairs of neighbouring frequencies, 5.0+8.4, 2.2+5.0 and 1.6+2.2 GHz, shown in Figs 8–10. For this purpose, we made images at both frequencies

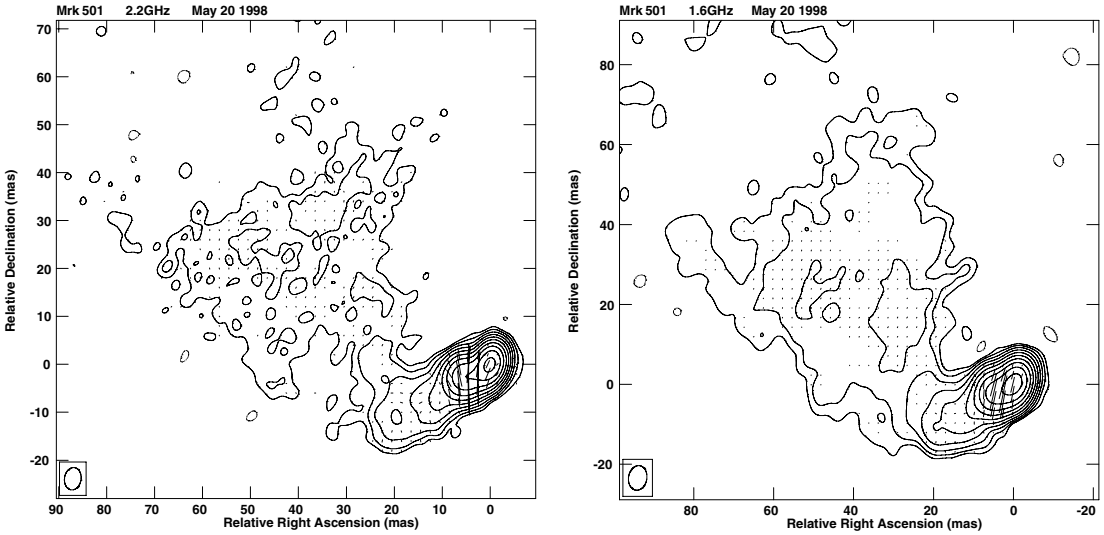

Figure 4. Inner part of the *I* images at 2.2 GHz (left-hand panel) and 1.6 GHz (right-hand panel) with superposed polarization ***E*** vectors. The ***E*** vectors have been rotated by $-\mathrm{RM}_{\mathrm{int}}\lambda^2 = -40^\circ$ (top) and $-\mathrm{RM}_{\mathrm{int}}\lambda^2 = -78^\circ$ (bottom) to remove the integrated Faraday rotation.

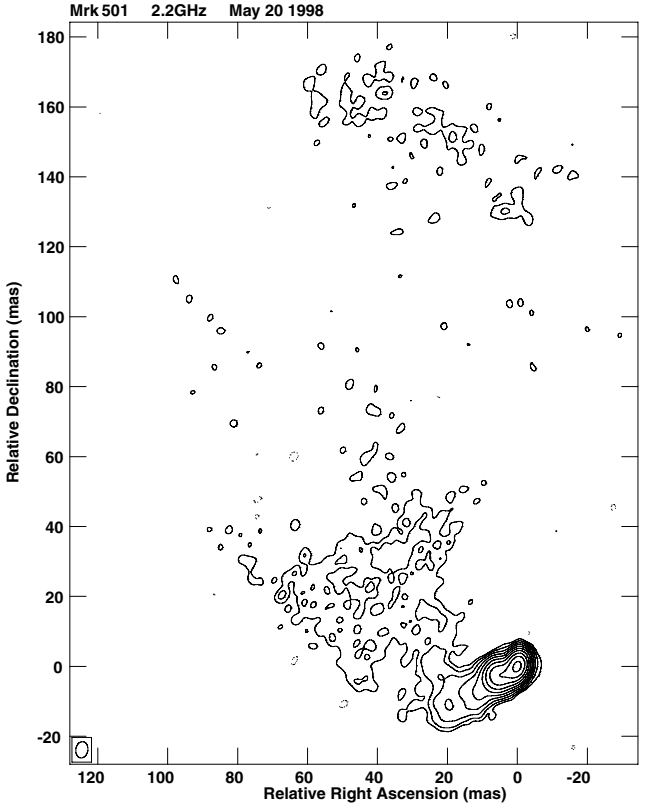

Figure 5. Contours of total intensity at 2.2 GHz, showing extended diffuse emission. The convolving beam has FWHM 4.69 × 3.45 mas and PA = −9.12°. The contour levels are −1, 1, 2, 4, 8, 16, 32, 64, 128, 256 and 512 mJy beam^{-1}, and the peak is 641.4 mJy beam^{-1}.

in a pair with the same pixel size and numbers of pixels, convolved with the same CLEAN beam, indicated in the image captions; the tapered 2.2 GHz image was used in the 1.6+2.2 GHz spectral index map. Since information about the absolute positions of the images is lost during the phase calibration of the data, we aligned the images relative to one another using the cross-correlation method described by Croke & Gabuzda (2008), which provides an objective estimation of the shift required to obtain the maximum cross-correlation coefficient between the entire optically thin region of the source detected at both frequencies (i.e. to align the images at the two frequencies). This approach is particularly valuable when there are no compact, easily distinguishable optically thin jet features detected at all frequencies of interest, as is the case with Mrk 501. We discuss and interpret the magnitudes of the core shifts derived below.

The spectral index maps were constructed using the AIPS task COMB, which calculates the spectral index α between a given pair of frequencies pixel by pixel. Note that the pair of frequencies 5.0+8.4 and 1.6+2.2 GHz were both observed on 1998 May 15 and 20, respectively; the 2.2- and 5-GHz data were obtained on different days, but, as we indicate above, we have found no evidence for variability of the source during the 5 days between the two observing sessions.

All three spectral index maps show the core to have a flat or somewhat inverted (partially optically thick) spectrum, while the jet has a relatively steep (optically thin) spectrum. The typical jet spectral indices are near −0.5 to −0.7 in the 5–8.4- and 2.2–5-GHz spectral index maps, but have increased to near 0.0 in the 1.6–2.2-GHz spectral index map, possibly suggesting an increased contribution from a component with a higher optical depth at the lower frequencies. All three maps display some regions in the jet where the spectrum appears to flatten. In the case of the 1.6–2.2-GHz spectral index map (Fig. 10), the observed jet spectral distribution in the extended jet is rather patchy, with regions of steep and inverted spectra surrounded by flat spectrum regions.

It is natural to ask if some of the observed features in the spectral index maps in Figs 8 to 10 could be artefacts associated with the application of incorrect shifts to align the images at the different frequencies. In test spectral index maps made using other shifts (including zero shift, i.e. aligning the maps on their *I* peaks), significant changes in spectral index occurred only in the immediate vicinity of the bright VLBI core, while the jet spectral index distribution in Figs 8–10 remained effectively unchanged. This was true for all spectral index maps produced using various test alignment shifts, and is very natural: the core region is far more sensitive to

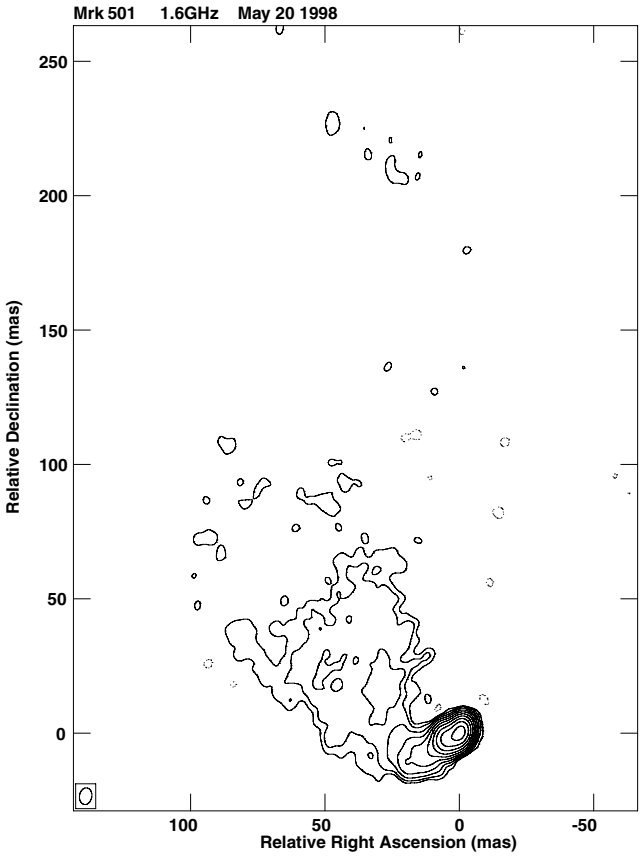

Figure 6. Contours of total intensity at 1.6 GHz, showing extended diffuse emission. The convolving beam has FWHM 6.20 × 4.58 mas and PA = −9.49°. The contour levels are −0.7, 0.7, 1.4, 2.8, 5.6, 11.2, 22.4, 44.8, 89.6, 179.2 and 358.0 mJy beam^{-1}, and the peak is 531.2 mJy beam^{-1}.

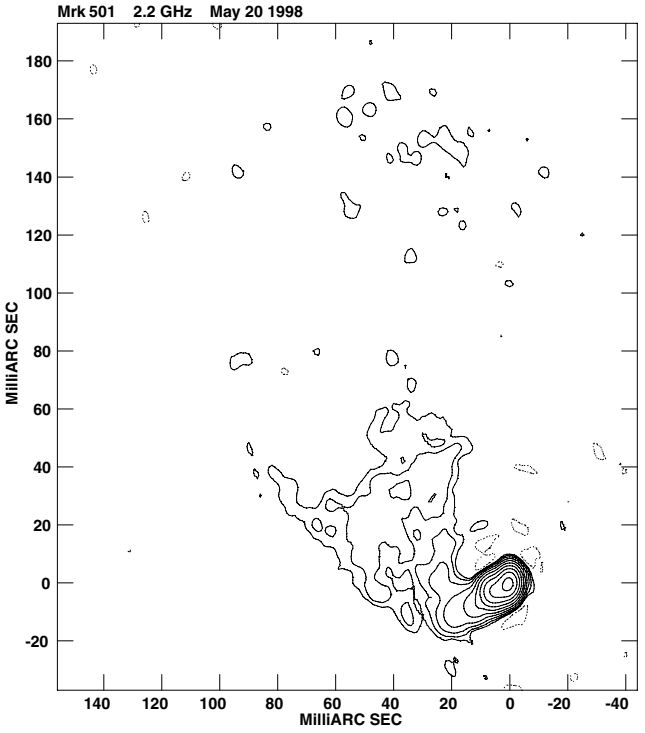

Figure 7. Contours of total-intensity tapered image at 2.2 GHz, showing extended diffuse emission. The convolving beam is the same as in the 1.6 GHz image. The contour levels are −1, 1, 2, 4, 8, 16, 32, 64, 128, 256 and 512 mJy beam^{-1}, and the peak is 683.6 mJy beam^{-1}.

changes in alignment between the maps, since the intensity gradient is largest here, as the intensity falls off from its peak.

Due to the low signal-to-noise ratio in the extended jet regions detected at 1.6 and 2.2 GHz, artefacts in the spectral index image can arise due to errors introduced during the mapping process such as redistribution of flux along positive side lobes of the dirty beam. Our tapering of the 2.2 GHz uv data to match the 1.6 GHz image resolution helped reduce the effect of side lobes and increase sensitivity to the extended jet emission, providing a more reliable spectral index distribution in low signal-to-noise ratio areas (Fig. 10). There is some evidence for regions of positive and negative spectral indices crossing the jet but spectral index images based on data with significantly weaker side lobes and much higher signal-to-noise ratio would be required to demonstrate whether this is due to real physical structures or not.

5.4 Faraday rotation

We constructed a RM map using the calibratedPANG maps for all four frequencies considered here using the AIPS task RM. In preparation for this, PANG noise (PANGN) maps were created together with the PANG maps from the Q and U maps at each frequency using the AIPS task COMB. The effect of the integrated (presumed Galactic) Faraday rotation was removed from the PANG maps, to ensure that any Faraday rotation observed in the final RM maps arises in the vicinity of the AGN (Rusk 1988; Pushkarev 2001).

The PANG and PANGN maps at all frequencies were assembled as a data cube before being passed to the task RM. The RM is calculated pixel-by-pixel in the task RM by fitting a straight line to a graph of $\chi_{\rm obs}$ versus λ^2 (the RM is the slope of this line).

Fig. 11 shows the RM distribution constructed from the 1.6, 2.2, 5 and 8.4 GHz PANG maps. This RM map shows a clear RM gradient across the jet, confirming the results of Gabuzda et al. (2004). The slice across the jet plotted in Fig. 11 (obtained with the AIPS task SLICE) shows that the change in RM is well outside the errors. Plots of $\chi_{\rm obs}$ versus λ^2 are also shown for three points along the slice; the error bars in these graphs correspond to the noise in the input maps. The $\chi_{\rm obs}$ versus λ^2 plots are all good fits to the data points, demonstrating the action of Faraday rotation and indicating that the jet $\boldsymbol{B}$ field is ordered on scales of the order of the beam size.

The line along which the maximum RM gradient is detected changes orientation with distance from the core, consistent with the curved trajectory of the jet. This RM map thus provides new, firm evidence for a helical $\boldsymbol{B}$ field associated with this jet.

We can use the RM map in Fig. 11 to correct the observed PANGs for Faraday rotation intrinsic to the source. This yields a map of the distribution of χ_0, the intrinsic EVPA, throughout the source. The AIPS task RM outputs a $\boldsymbol{B}$-field map together with the RM map, which corresponds to the orientation of the local $\boldsymbol{B}$ field calculated from the derived χ_0 values, assuming that the local $\boldsymbol{B}$ field is everywhere orthogonal to the local χ_0. In order not to make this last assumption, we rotated the angles in the $\boldsymbol{B}$-field map by 90° to obtain instead the distribution of χ_0.

Fig. 12 shows this χ_0 distribution superposed on the 1.6-GHz I map. The 'spine + sheath' polarization structure is clearly visible. The clear reproduction of this spine and sheath structure and the high degree of order seen here and in the RM fits serves to

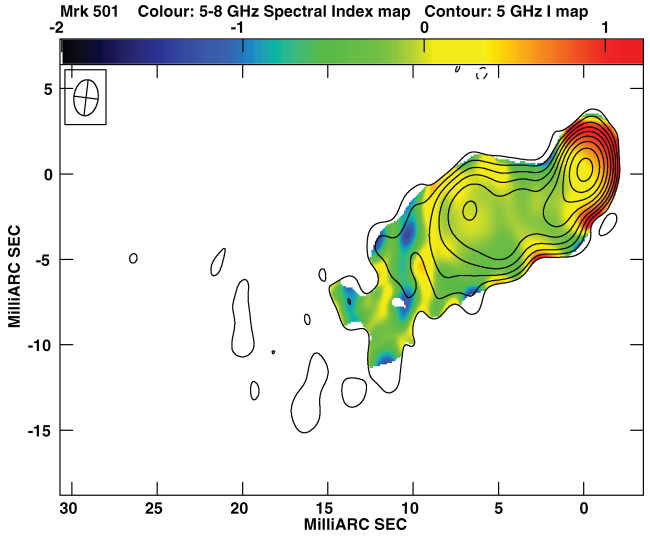

Figure 8. Spectral index distributions constructed from 5.0- and 8.4-GHz data. The two I maps were both convolved with a beam with FWHM 2.5 × 1.5 mas and PA $= -6^\circ$ (corresponding to the 5 GHZ beam). The contours of total intensity at 5 GHz are superimposed. The contour interval is a factor of 2, with the lowest contour level being 1.6mJy beam^{-1} and a peak intensity of 524.6 mJy beam^{-1}. The colour scale ranges from $-2 < \alpha < 1.2$. Clip levels of I maps: 1.6 mJy (5.0 GHz), 1.3 mJy (8.4 GHz).

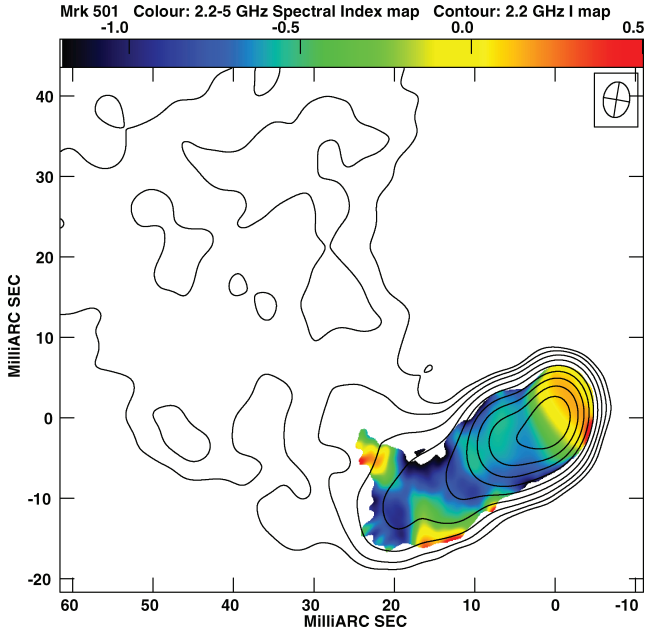

Figure 9. Spectral index distributions constructed from 2.2- and 5.0-GHz data. The two I maps were both convolved with a beam with FWHM 4.5 × 3.5 mas and PA $= -9^\circ$ (corresponding to the 2.2-GHz beam). The contours of total intensity at 2.2 GHz are superimposed. The contour interval is a factor of 2, with the lowest contour level being 1.4 mJy beam^{-1} and a peak intensity of 683.6 mJy beam^{-1}. The colour scale ranges from $-1.2 < \alpha < 0.5$. Clip levels of I maps: 2.4 mJy (2.2 GHz), 1.6 mJy (5.0 GHz).

reassure us of the correctness of the EVPA calibrations for the 2.2- and 1.6-GHz PANGs. In addition, the 'sheath' of orthogonal polarization remains orthogonal to the jet as it undergoes its dramatic $\simeq 90^\circ$ bend. The 'spine' of aligned polarization vectors can be seen most clearly just before this bend. The direction of the polarization beyond the bend, in the diffuse northern part of the jet, is less

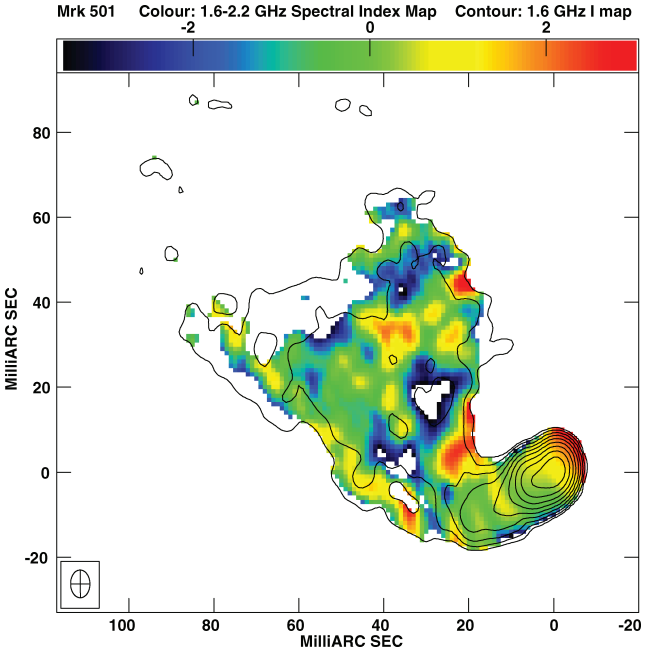

Figure 10. Top: spectral index distribution constructed from the 1.6 and tapered 2.2 GHz images. The two I maps were both convolved with a beam with FWHM 6.0 × 4.5 mas and PA $= -10^\circ$ (corresponding to the 1.6-GHz beam). The contours of total intensity at 1.6 GHz are superimposed. The contour interval is a factor of 2, with the lowest contour level being 1.0 mJy beam^{-1}. The colour scale ranges from $-3.5 < \alpha < 3$. Clip levels of I maps: 1.0 mJy (1.6 GHz), 0.9 mJy (2.2 GHz).

clear, but may be roughly aligned with the jet structure, as would be expected if this polarization were due to the toroidal component of a helical jet $\boldsymbol{B}$ field. Thus, the polarization structures before and beyond the $\simeq 90^\circ$ are both consistent with the presence of a helical $\boldsymbol{B}$ field associated with the jet of Mrk 501. The polarization structure in this image is qualitatively similar to the one presented in Giroletti et al. (2008) at 1.4 GHz. However, a detailed comparison with regard to the orientation of the EVPAs is not possible since they did not have sufficient observations to remove the highly significant effect of Faraday rotation at these low frequencies.

5.5 The core shift and core magnetic field in Mrk 501

The standard theory of extragalactic radio sources (Blandford & Königl 1979) predicts a frequency-dependent shift in the location of the VLBI core due to opacity effects near the base of the jet. The reabsorption of synchrotron radiation that takes place in the ultracompact region near the central engine of an AGN is more efficient at low frequencies. Consequently, the peak brightness appears further along the jet axis in lower frequency observations. For this reason, aligning multifrequency images by their peaks (effectively, on their VLBI cores) results in a misalignment between images at different observing frequencies. The frequency-dependent shift in core position has been measured for several quasars and microquasars (Lobanov 1998, and references therein).

From the jet model of Blandford & Königl (1979) and Königl (1981), the frequency dependence of the self-absorbed core is described by $r \propto \nu^{-1/k_r}$, where r is the distance from the central engine and $k_r = [(3 - 2\alpha)m + 2n - 2]/(5 - 2\alpha)$, with m and n describing the power-law decreases in the magnetic field and particle density, respectively, with distance from the central engine. For

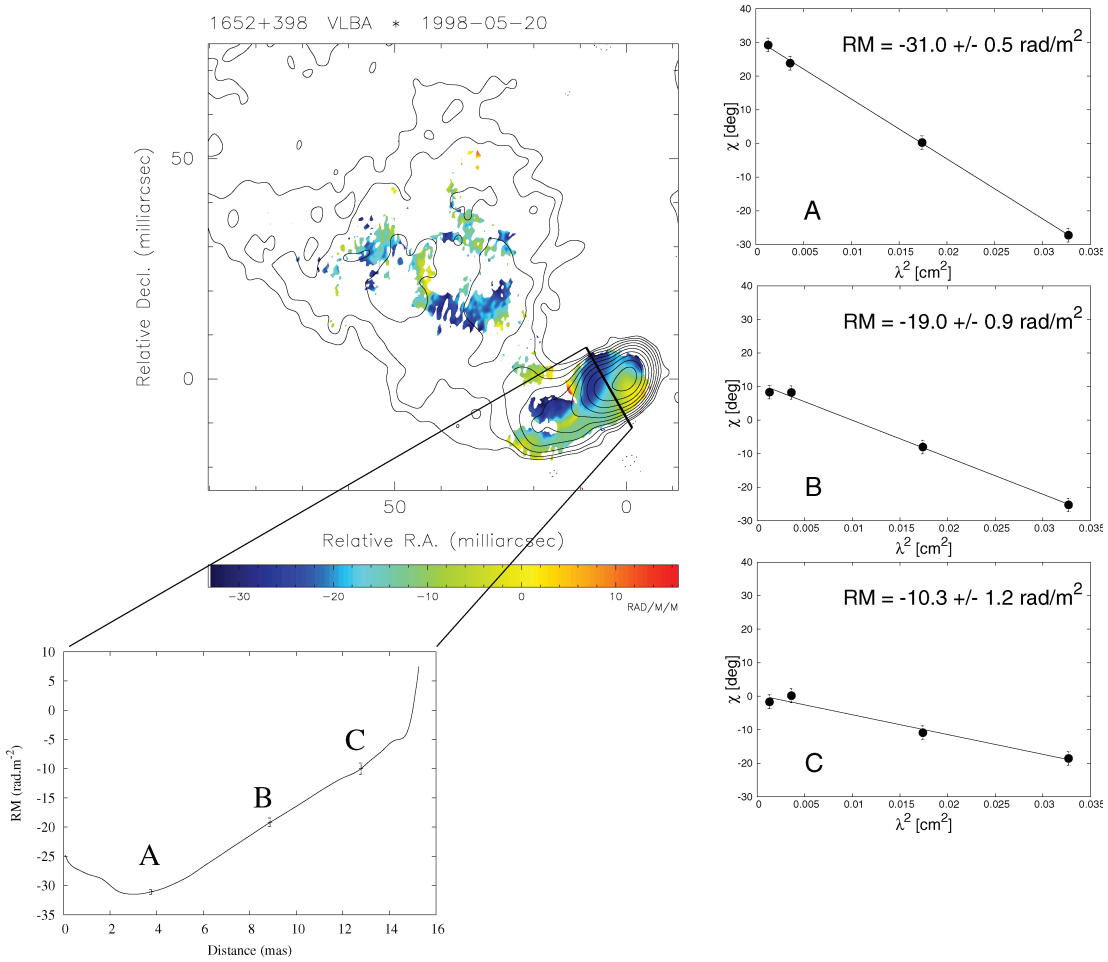

Figure 11. RM map constructed from 1.6- and 2.2-GHz data observed on 1998 May 20 and 5- and 8.4-GHz data observed on 1998 May 15. The four PANG maps were convolved with a beam FWHM 6.0 × 4.5 mas, PA = −10° (corresponding to the 1.6-GHz beam size). The contours of total intensity at 1.6 GHz are superimposed. The contours increase in steps of a factor of 2 from the lowest level of 0.7 mJy beam^{-1}. The plot on the bottom left shows the profile of the RM distribution across the indicated slice on the map, and the fits obtained at the points A, B and C along the slice are shown in the plots on the right-hand side.

equipartition between the jet particle and magnetic field energy densities, $k_r = 1$, independent of the spectral index. Although various combinations of m and n could, in principle, give this result, the choice of $m = 1$ and $n = 2$ corresponds to the simplest case (e.g. Hutter & Mufson 1986; Lobanov 1998). Therefore, in equipartition, the core shift ($\Delta r = r_{\nu_1} - r_{\nu_2}$) between two frequencies ($\nu_2 > \nu_1$) becomes directly proportional to $(\nu_2 - \nu_1)/(\nu_2\nu_1)$. Lobanov (1998) discusses in detail how the frequency dependence of the shift depends on the physical conditions near the central engine. Katarzyński, Sol & Kus (2001) estimated the values $m = 0.9$ and $n = 1.8$ for Mrk 501, confirming the appropriateness of using the values $m = 1$ and $n = 2$.

As is noted above, we applied the cross-correlation program of Croke & Gabuzda (2008) to pairs of our images at various frequencies constructed with matched parameters. The results are summarized in Table 3. The uncertainties in the RA and Dec. shifts correspond to half the pixel sizes for the images used to derive the shifts, which were 0.10 mas for all cases except the 5.0–8.5 GHz shift, which was found using maps with 0.05 mas pixel^{-1}. The derived shifts in RA and Dec are also all multiples of half a pixel size. This is so because the alignment program of Croke & Gabuzda (2008) blocks out a specified number of beam areas around the core; in some cases, blocking out different numbers of beam areas (e.g. 2.5 or 3.0) yielded slightly different shifts (e.g. differing by 1 pixel), which, in turn, yielded spectral index maps that clearly slightly overestimated the correct shift in one case and slightly underestimated it in the other case. In these cases, we adopted the intermediate shift between the two as our best estimate of the shift in that coordinate, after verifying that this yielded improved (more monotonic) behaviour of the spectral index map in the core region. (Note that we are able to do this because the AIPS task OGEOM is capable of realizing an image shift by as little as half a pixel.) Our shifts are consistent with those of Giroletti et al. (2004): we measured a core shift of 0.72 ± 0.28 mas from their 5-GHz ground VLBI and 1.6-GHz space VLBI images (kindly provided by M. Giroletti), which they independently aligned using the positions of the optically thin jet components. They were able to do this because their space VLBI observations at 1.6 GHz had a similar resolution to the ground-based 5-GHz image.

Plotting the measured core shifts for our multifrequency observations of Mrk 501 versus the frequency parameter $(\nu_2 - \nu_1)/(\nu_2\nu_1)$ (Fig. 13) shows that the data are described well by a linear

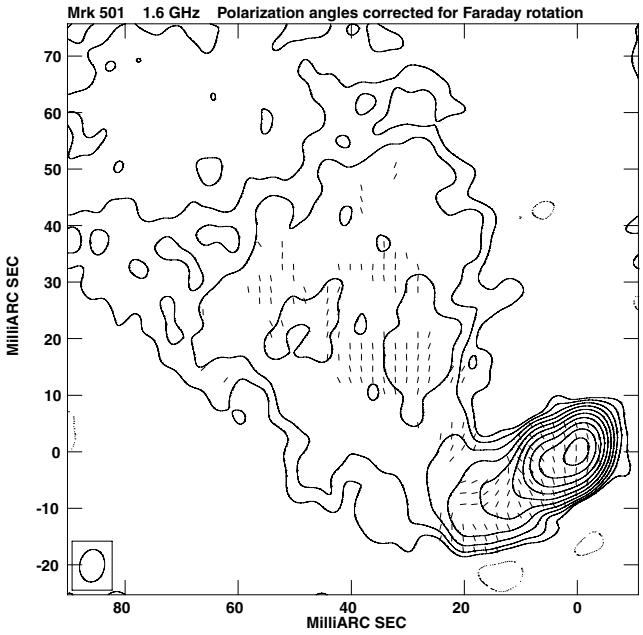

Figure 12. Direction of linear polarization in Mrk 501, corrected for local rotation using the RM distribution map shown in Fig. 11. Contours of total intensity at 1.6 GHz are shown, levels increase by a factor of 2 at each contour, from the lowest level of 0.7 mJy beam^{-1}.

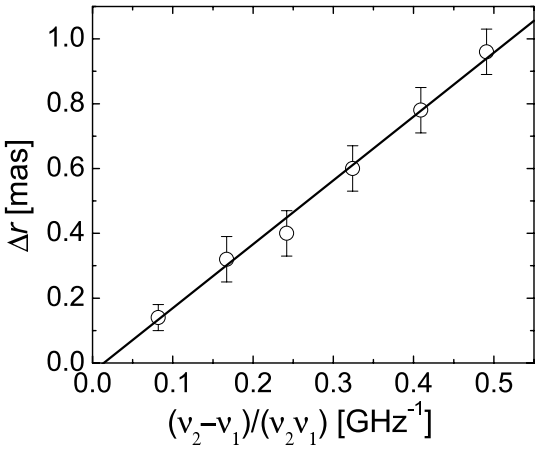

Figure 13. Plot of the measured core shift versus the frequency parameter $(\nu_2 - \nu_1)/(\nu_2\nu_1)$. The points for a jet in equipartition should display a linear dependence that passes through the origin. The straight line fitted to the data has a y intercept of -0.03 ± 0.05 mas, showing that the jet of Mrk 501 is well described by the equipartition value of $k_r = 1$ from 1.64 to 8.41 GHz.

relationship that passes through the origin. No significant deviations from linear behaviour are observed, as would arise if k_r were not equal to unity throughout the observed frequency range. The formal y-intercept of the fit is -0.03 ± 0.05, which is consistent with zero within 1σ. Our core shifts accordingly represent a direct observational measurement indicating that the part of the jet corresponding to the observed VLBI core region is close to equipartition between 1.6 and 8.4 GHz.

Comprehensive multi-epoch, multifrequency VLBI observations (see Giroletti et al. 2004, and references therein) have provided some of the best estimates of the source geometry. The estimated viewing angle is in the range $15^\circ < \theta_j < 20^\circ$. The jet is strongly relativistic, with an estimated bulk Lorentz factor $\gamma_j \sim 15$. The

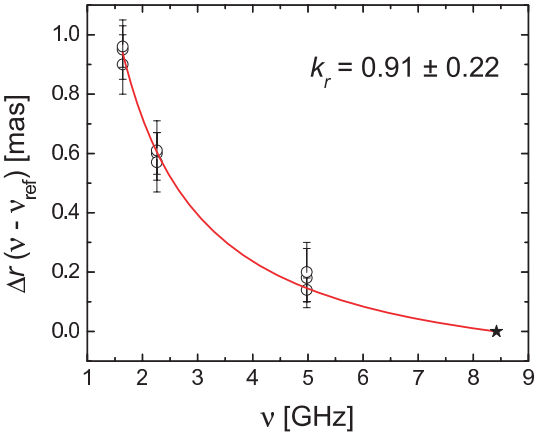

Figure 14. Plot of core-shift measurements versus frequency for all possible frequency combinations, using 8.41 GHz as the reference frequency. The best-fitting line has $\Delta r = A(\nu^{-1/k_r} - 8.41^{-1/k_r})$ with parameters $A = 1.9 \pm 0.2$ and $k_r = 0.91 \pm 0.22$.

measured constant opening angle of $\sim 40^\circ$ out to more than 500 mas implies an intrinsic jet opening angle $\phi_j \sim 10^\circ$–15°.

Following the analyses of Lobanov (1998) and Hirotani (2005), we are able to derive estimates for the magnetic field at a distance of 1 pc, B_1, and the magnetic fields in the 1.6, 2.2, 5 and 8.4 GHz cores, $B_{\rm core}(\nu)$, along with their respective distances from the central engine, $r_{\rm core}(\nu)$. We adopt a jet spectral index of $\alpha_j = -0.7$, consistent with our own spectral index maps. Even though the jet spectral index between 1.6 and 2.2 GHz is flat, we still use $\alpha = -0.7$ to describe the emission from the relativistic electrons in the unresolved core region at these frequencies because we are modelling the optically thin emission from the compact inner jet region used to describe the core, and hence the highest resolution images provide the best estimate of the spectrum in this region. To describe the core region, we use the values $\phi_j = 10^\circ$, $\gamma_j = 15$, $\theta_j = 15^\circ$, corresponding to $\delta_j = 2$ (see Giroletti et al. 2008). The redshift of Mrk 501 corresponds to a luminosity distance (D_L) of 146.1 Mpc for the cosmology adopted here.

The magnetic field strength depends on the lower cut-off of the electron-energy distribution ($\gamma_{\rm min}$) as $B_1 \propto \gamma_{\rm min}^{-0.095}$ for $\alpha = -0.7$ (see O'Sullivan & Gabuzda 2009). For a jet dominated by an electron–proton plasma, the energy distribution must have a cut-off of $\gamma_{\rm min} \leq 100$ (Ghisellini et al. 1992; Wardle et al. 1998), while, for an electron–positron jet, $\gamma_{\rm min}$ can extend all the way down to 1 (Reynolds et al. 1996; Hirotani 2005). Table 4 lists our estimates of B_1, $B_{\rm core}$ and $r_{\rm core}$ based on the above parameters and our observed core shifts, assuming $\gamma_{\rm min} = 100$. We also list the core position offset measure, $\Omega_{r\nu}$, for comparison with those given by Lobanov (1998). The magnetic field strengths can easily be converted for other values of $\gamma_{\rm min}$, since $r_{\rm core}$ remains unaffected and $B_{\rm core}(\nu) = B_1\, r_{\rm core}^{-1}$ for the case of equipartition. For $\gamma_{\rm min} = 100$, we have an average $B_1 = 0.04 \pm 0.01$ G and for $\gamma_{\rm min} = 1$, we find $B_1 = 0.07 \pm 0.02$ G. Using the equipartition condition, we find the jet particle number density varies from 61 to 0.23 cm^{-3} for values of $\gamma_{\rm min}$ from 1 to 100.

The physical parameters of the inner jet of Mrk 501 have been estimated by several authors over the last $\sim$25 years, based on broadband observations from radio to γ-ray. Synchrotron self-Compton (SSC) and relativistic-jet models applied to X-ray, ultraviolet, optical and radio observations by Mufson et al. (1984), and Hutter & Mufson (1986) provided the earliest estimates of the jet parameters.

Table 3. Observed core shifts in Mrk 501.

ν_1 (GHz)	ν_2 (GHz)	RA shift (mas)	Dec. shift (mas)	Δr (mas)	Direction (°)	Fraction of beam size
4.98	8.41	0.10 ± 0.03	0.10 ± 0.03	0.14 ± 0.04	-45 ± 9	5%
2.26	4.98	0.20 ± 0.05	0.35 ± 0.05	0.40 ± 0.07	-30 ± 9	7%
2.26	8.41	0.40 ± 0.05	0.45 ± 0.05	0.60 ± 0.07	-42 ± 5	11%
1.64	2.26	0.20 ± 0.05	0.25 ± 0.05	0.32 ± 0.07	-39 ± 9	4%
1.64	4.98	0.55 ± 0.05	0.55 ± 0.05	0.78 ± 0.07	-45 ± 3	11%
1.64	8.41	0.70 ± 0.05	0.65 ± 0.05	0.96 ± 0.07	-47 ± 3	13%

Table 4. Magnetic field estimates for Mrk 501.

ν (GHz)	$\Omega_{r\nu}$ (Gpc Hz^{-1})	B_1 (G)	$B_{\rm core}(\nu)$ (G)	$r_{\rm core}\nu$ (pc)
8.41	1.16 ± 0.18	0.04 ± 0.01	0.079 ± 0.006	0.5 ± 0.1
4.98	1.08 ± 0.14	0.04 ± 0.01	0.048 ± 0.003	0.8 ± 0.1
2.26	1.23 ± 0.28	0.04 ± 0.01	0.021 ± 0.002	2.1 ± 0.5
1.64	-	0.04 ± 0.01	0.014 ± 0.002	3.3 ± 0.7

Note. Only errors in the core-shift measurements are considered. The magnetic field strengths are calculated for $\gamma_{\rm min} = 100$. The physical parameters at 1.64 GHz are calculated using the 2.26 GHz core-position offset measure.

They found a magnetic field strength of $B_1 = 0.09$ G and a particle density of $N_1 = 140$ cm^{-3} using $\phi_{\rm j} = 5°$, $\gamma_{\rm j} = 10$, $\theta_{\rm j} = 25°$ and $\delta_{\rm j} = 1.1$. Using these jet parameters in our model, we find $B_1 = 0.05 \pm 0.02$ G and $N_1 = 0.35$ cm^{-3} for $\gamma_{\rm min} = 100$ and $B_1 = 0.08 \pm 0.02$ G and $N_1 = 90$ cm^{-3} for $\gamma_{\rm min} = 1$. More recently, X-ray and γ-ray observations have set further constraints on the physical parameters of Mrk 501 (see Tavecchio et al. 2001; Katarzyński et al. 2001, and references therein). Using a 'blob-in-jet' scenario, where an SSC-emitting homogeneous plasma blob is embedded in a radio-emitting jet, Katarzyński et al. (2001) calculate a magnetic field strength of 0.35 G at the base of the jet, which would approximately correspond to the magnetic field strength in the 43-GHz core of Mrk 501 by extrapolation from our model. They also derive values of $m = 0.9$ and $n = 1.8$, justifying our assumption of the values $m = 1$ and $n = 2$. Giroletti et al. (2004) estimate magnetic field strengths of the order of tens of mG in the radio core, based on measurements of a spectral turnover in the core region at 8.4 GHz (e.g. Marscher 1987), in general agreement with our values calculated here.

6 CONCLUSIONS

We have presented polarization VLBI observations of Mrk 501 at 5, 8.4, 2.2 and 1.6 GHz. Our images reproduce the well-known complex VLBI intensity structure. Extended emission can be seen at 1.6 and 2.2 GHz, at about 160–180 mas from the core; this region of enhanced emission is shown to be at the north-western edge of the jet in the deep 1.6-GHz image of Giroletti et al. (2008).

The 'spine–sheath' polarization structure previously noted for this source is dominated by the sheath at our epoch, with the spine seen most clearly in the inner jet at 8 GHz. The polarization structure at 1.6 and 2.2 GHz also displays a spine–sheath structure that can be traced to ∼30 mas from the core. After correction for Galactic and local Faraday rotation, the sheath polarization $\boldsymbol{E}$ vectors remain orthogonal to the jet even as it undergoes an almost 90° bend ∼30 mas from the core. The spine of aligned polarization can be seen just before this bend, and also changes direction to remain aligned with the jet.

The spectral index distribution of the source is complex, with large variations in spectral index along and across the jet visible for all three pairs of neighbouring frequencies. We have determined the positions of the radio cores at each frequency relative to our highest frequency by carrying out a cross-correlation analysis of the optically thin jet emission using the method of Croke & Gabuzda (2008). The derived position of the radio core from the base of the jet follows the law $r_{\rm core}(\nu) \propto \nu^{-1.1\pm0.2}$, consistent with the jet being in equipartition. The inferred core $\boldsymbol{B}$ fields in this case are $B_1 \simeq 0.04$ G and $0.01 \leq B_{\rm core}(\nu) \leq 0.08$ G for the frequency range from 1.6 to 8.4 GHz. These values are consistent with the results of Katarzyński et al. (2001) and Giroletti et al. (2004).

We have presented the first RM map of which we are aware based on a joint analysis of polarization data at 1.6, 2.2, 5 and 8 GHz. There is a clear systematic gradient in the RM across the VLBI jet, extending from the core region to a distance of about 30 mas from the core. This confirms the previous detection of such a RM gradient based on observations at 5, 8 and 15 GHz (Gabuzda et al. 2004) and provides new support for the hypothesis that a helical magnetic field is associated with the jet of Mrk 501.

ACKNOWLEDGMENTS

Funding for part of this research was provided by the Irish Research Council for Science, Engineering and Technology. The authors would like to thank the referee for constructive criticism that improved this paper. The VLBA is a facility of the NRAO, operated by Associated Universities Inc. under cooperative agreement with the NSF. This research has made use of the VLA polarization monitoring program as well as data from the UMRAO, which is supported by the NSF and by funds from the University of Michigan. This research has also made use of NASA's Astrophysics Data System Service.

REFERENCES

Aaron S., 1999, in Takalo L. O., Sillanpää A., eds, ASP Conf. Ser. Vol. 159, The BL Lac Phenomenon. Astron. Soc. Pac., San Fransisco, p. 427
Blandford R. D., Königl A., 1979, ApJ, 232, 34
Cassaro P., Stanghellini C., Bondi M., Dallacasa D., DellaCeca R., Zappala R. A., 1999, A&AS, 139, 601
Charlot P., Gabuzda D. C., Sol H., Degrange B., Piron F., 2006, A&A, 457, 455
Conway J. E., Wrobel J. M., 1995, ApJ, 439, 98
Croke S. M., Gabuzda D. C., 2008, MNRAS, 386, 619
Djannati-Ataı A. et al., 1999, A&A, 350, 17
Edwards P. G., Piner B. G., 2002, ApJ, 579, L67
Gabuzda D. C., Chernetskii V. A., 2003, MNRAS, 339, 669

Gabuzda D. C., Pushkarev A. B., Cawthorne T. V., 2000, MNRAS, 319, 1109
Gabuzda D. C., Murray É., Cronin P., 2004, MNRAS, 351, L89
Ghisellini G., Celotti A., George I. M., Fabian A. C., 1992, MNRAS, 258, 776
Giommi P., Padovani P., 1994, MNRAS, 268, L51
Giovannini G., Feretti L., Venturi T., Cotton W. D., Lara L., 1999, in Takalo L. O., Sillanpää A., eds, ASP Conf. Ser. Vol. 159, The BL Lac Phenomenon. Astron. Soc. Pac., San Fransisco, p. 439
Giroletti M. et al., 2004, ApJ, 600, 127
Giroletti M., Giovannini G., Cotton W. D., Taylor G. B., Pérez-Torres M. A., Chiaberge M., Edwards P. G., 2008, A&A, 488, 905
Hallahan D. R., Gabuzda D. C., 2008, in Proceedings of the Workshop on Blazar Variability Across the Electromagnetic Spectrum. Published online at http://pos.sissa.it, p. 40
Hirotani K., 2005, ApJ, 619, 73
Hughes P. A., Aller H. D., Aller M. F., 1989, ApJ, 341, 68
Hutter D. J., Mufson S. L., 1986, ApJ, 301, 50
Katarzyński K., Sol H., Kus A., 2001, A&A, 367, 809
Kharb P., Gabuzda D., Shastri P., 2008, MNRAS, 384, 230
Kollgaard R. I., Wardle J. F. C., Roberts D. H., Gabuzda D. C., 1992, ApJ, 104, 1687
Königl A., 1981, ApJ, 243, 700
Laing R. A., 1980, MNRAS, 193, 439
Lipovetsky V. A., Makarian B. E., Stepanian J. A., 1987, in Khachikian E. E., Fricke K. J., Melnick J., eds, Proc. IAU Symp. 121, Observational Evidence of Activity in Galaxies. Kluwer, Dordrecht, p. 17
Lobanov A. P., 1998, A&A, 330, 79
Lyutikov M., Pariev V. I., Gabuzda D. C., 2005, MNRAS, 360, 869
Marscher A. P., 1987, in Zensus J. A., Pearson T. J., eds, Superluminal Radio Sources, Vol. 280. Cambridge Univ. Press, Cambridge
Mufson S. L. et al., 1984, ApJ, 285, 571
O'Sullivan S. P., Gabuzda D. C., 2009, MNRAS, 400, 26
Padovani P., Giommi P., 1995, ApJ, 444, 567
Pushkarev A. B., 2001, Astron. Rep., 45, 667
Pushkarev A. B., Gabuzda D. C., Vetukhnovskaya Yu. N., Yakimov V. E., 2005, MNRAS, 356, 859
Reynolds C. S., Fabian A. C., Celotti A., Rees M. J., 1996, MNRAS, 283, 873
Reynolds C., Cawthorne T. V., Gabuzda D. C., 2001, MNRAS, 327, 1071
Rusk R., 1988, PhD thesis, Univ. Toronto
Spitzer L. Jr, 1978, Physical Processes in the Interstellar Medium. Wiley, New York
Sturrock P. A., 1994, Plasma Physics. Cambridge Univ. Press, Cambridge
Tavecchio F. et al., 2001, ApJ, 554, 725
Ulrich M.-H., Kinman T. D., Lynds C. R., Rieke G. H., Ekers R. D., 1975, ApJ, 198, 261
Wardle J. F. C., Homan D. C., Ojha R., Roberts D. H., 1998, Nat, 395, 457
Wright E. L., 2006, PASP, 118, 1711
Yamamoto T. et al., 1999, preprint (astro-ph/9906055)
Zavala R. T., Taylor G. B., 2003, ApJ, 589, 126

This paper has been typeset from a TEX/LATEX file prepared by the author.